Multiscale power fluctuation evaluation of a hydro-wind-photovoltaic system

Hualin Xiong[a,b], Beibei Xu[a,b], Xingqi Luo[d], Xingjin Zhang[a,b], Edoardo Patelli[c], Pengcheng Guo[d], Diyi Chen*[a,b]

[a]*Institute of Water Resources and Hydropower Research, Northwest A&F University, Shaanxi Yangling 712100, P. R. China*

[b]*Key Laboratory of Agricultural Soil and Water Engineering in Arid and Semiarid Areas, Ministry of Education, Northwest A & F University, Shaanxi Yangling 712100, P. R. China*

[c]*Centre for Intelligent infrastructure, Department of Civil and Environmental Engineering, University of Strathclyde, 75 Montrose Street, Glasgow, G1 1XJ, UK*

[d]*State Key Laboratory Based of Eco-hydraulic Engineering in Arid Area, Xi'an University of Technology, Xi'an 710048, Shaanxi, P. R. China*

***Corresponding author:** Diyi Chen

Mailing Address: Institute of Water Resources and Hydropower Research, Northwest A&F University, Shaanxi Yangling 712100, China

Telephones: 086-181-6198-0277

E-mail: diyichen@nwsuaf.edu.cn

Abstract: Hybrid energy systems need to operate in stable condition across different time scales. Studies on the stability of such systems are carried out under the unrealistic assumption of discontinuous time scale. To overcome the current limitations of the stability evolution law for hybrid power system, this study propose a second time scale model. Three indicators, including the power spectral density, stability index and complementary index, are adopted to investigate the stability characteristics of the hybrid system with the time scale varying from second to day. In addition, the obtained characteristics are compared with or without hydropower compensation. The results show that the volatility of wind power and photoelectric increase with the increase of time scale. In $(10^{-1}, 10^{0.5})$ seconds and $(10^{1}, 10^{1.5})$ seconds hydropower has the best compensation effect for wind and photoelectricity power and the compensation effect remains basically unchanged when the time scale is over $10^{1.5}$ seconds. The obtained stability evolution law has important reference significance for the subsequent studies on the stability of hybrid energy systems.

Keywords: hybrid energy system; continuous time scale; stability evaluation; hydropower complementation

1. Introduction

Hybrid energy systems combine and integrate different energy generation systems to exploit the advantage of different technologies and compensate for their deficiencies and they represent a

promising sustainable solution for power generation. For a successful application of such technology the stability of a hybrid energy system, i.e. the ability to return to the system's equilibrium after being disturbed[1], must be guaranteed. A hybrid energy systems with a stable power grid frequency is essential to industrial power consumptions; at the ecological level, a good stability performance indicates that the power system absorbs power generations of renewable energies preferentially to protect the ecology by reducing the proportion of non-renewable energies; at the economic level, it determines the capacity ratio of wind energy and solar energy. Therefore, it is necessary to study the stability of the hybrid energy system.

To solve the stability problem of integrated large-scale renewable energies power systems, scholars proposed many different methods in the area of power quality, coordinated control strategy and optimized scheduling from time scales of seconds to minutes and hours. Specifically, most studies focus on the power quality in the power grid frequency [2], voltage deviation [3, 4], power grid harmonic [5] and safe operation[6] for controlling the stability at the time scale of seconds. Rapid fluctuations in wind and photovoltaic power mainly affects the transient process of power system, especially the frequency and voltage of power system transient response. Zhang predicted the hydraulic compensation of photovoltaic power generation fluctuations and considered the effect of complementary regulation on power quality [7]. In [8], the effects of grid voltage distortion and imbalance had been detached by using complex vector filter-based synchronization technique. For minute-level time scale, the current research focuses on various control strategies [9, 10] and safe operation of the unit [11]. In [12], compensation units were introduced into the automatic power generation control system to reduce the influence of photovoltaic power output fluctuations. For hour-level time scale, many studies involving optimized scheduling have focused on short-term grid dispatching [13] and reducing the operating cost of renewable energy and the abandonment of water in reservoirs [14], improving ecological efficiency [15]. Sumit Banerjee et al. focused on the solving method of multi-energy power system [16]. Luis Ignacio Levieux et al. aimed to analyze the complementary operation between existing hydropower stations and wind farms [17]. Wang et al. proposed a coordinated operation model of power systems with hydro-thermal-wind-photovoltaic power considering the comprehensive utilization of reservoirs [18].

The above mentioned strategies for improving power quality, coordinated control strategy and optimal dispatch assume independent time scales. However, this discontinuity assumption cannot reflect the evolution of the stability of hybrid energy systems across different time scales. Therefore, this study focuses on the coupling of dynamic evolution of the hybrid energy systems with continuous time scale. Specific innovation points of this study are summarized as follows:

- A hydropower system is proposed to regulate wind and photoelectric power fluctuation, producing a hydro-wind-photovoltaic system;
- To reveal the suppression effect of hydropower stations on power fluctuations in power grid, the power spectral density method is used to compare change rules in the frequency domain of wind power, photoelectric power, and with or without hydropower regulation;
- Based on the introduced wind-water interconnection system, a stability and complementary evaluation method is proposed. The method focuses on describing the stability and complementary evolution law of quantized hydropower stations from second to hour.

This paper is structured as following. We introduced the hydro-wind-photovoltaic system in Section 2. In Section 3, the mathematical model of hydro-wind-photovoltaic system are studied. In Section 4, We use power spectral density, stability index and complementary index to analyze the

evolution law of hydro-wind-photovoltaic system's stability and complementary in different meteorological conditions from second to hour. Finally, the conclusion is given in Section 5.

2. Hydro-wind-photovoltaic system

The scheme of a Hydro-Wind-Photovoltaic System (HWPS) is shown in Fig. 1, which is mainly composed of the Hydropower Power Generation subsystem (HPG), the Photovoltaic Power Generation subsystem (PVPG) and the Wind Power Generation subsystem (WPG). The used HPG in HWPS is to mitigate the power fluctuations from PVPG and WPG by the coordinated controller. The expression of the coordinated controller is

$$V_p = P_{set} - P_W - P_S . \tag{1}$$

Where V_p is the power demand fed back to HPG; P_{set} is the given power from the electric power dispatching center; P_W is the output power of WPG; P_S is the output power of PVPG.

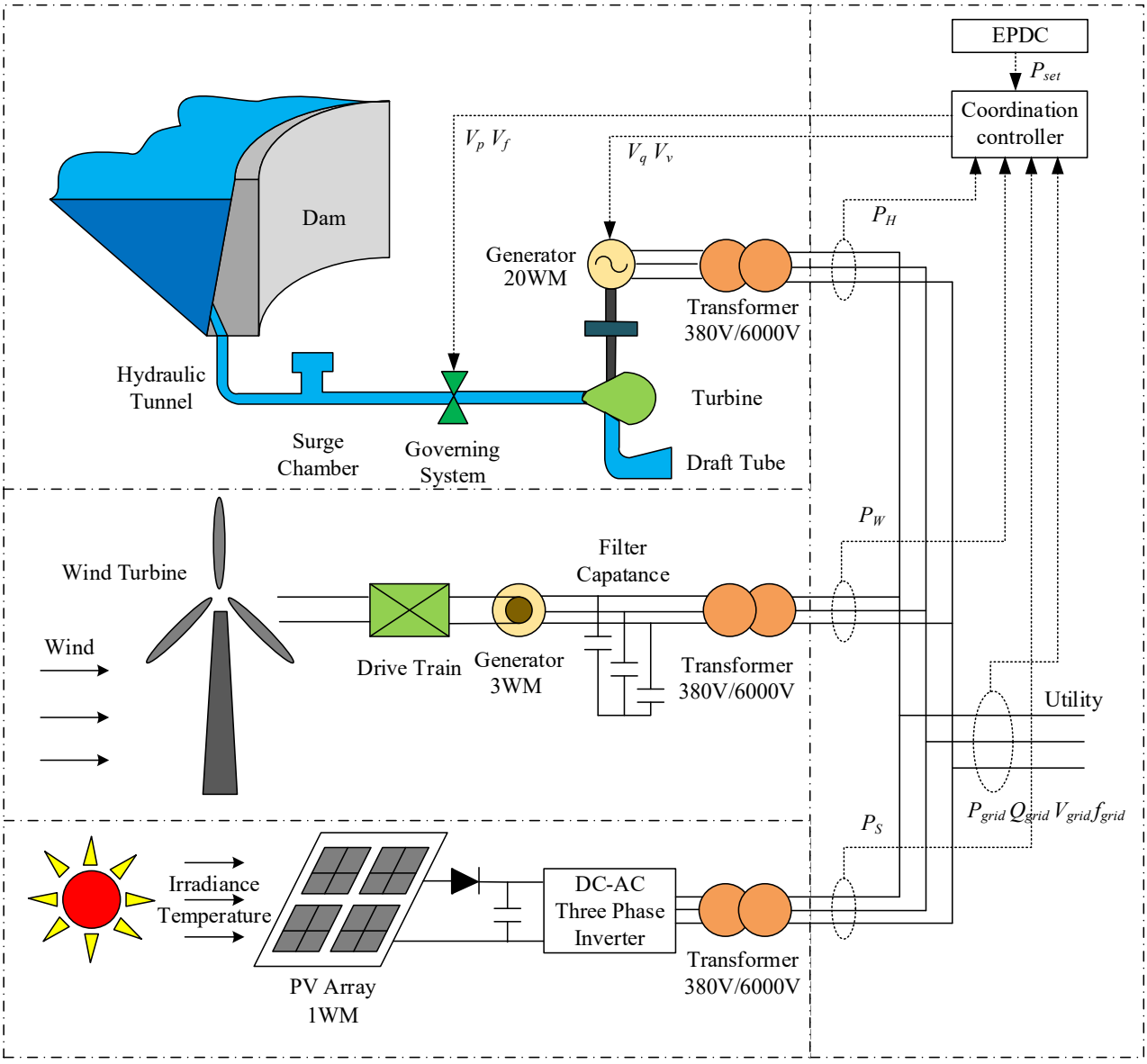

Fig.1. The structure of the Hydro-Wind-Photovoltaic System (HWPS). EDPC is the electric power dispatching center. P_{set} is the given power from EPDC; P_H is the output power of HPG; P_W is the output power of WPG; P_S is the output power of PVPG; P_{grid} is the total power of HWPS; Q_{grid}, V_{grid}, and f_{grid} are the reactive power, the voltage,

and the frequency of the grid in HWPS, respectively. V_q and V_v are the reactive power deviation and the voltage deviation signals fed back to HPG, respectively; V_p and V_f are the power deviation and the frequency deviation signals fed back to HPG, respectively.

2.1 HPG model

2.1.1 Pressure pipeline

The continuity equation and momentum equation are used to describe the dynamic characteristics of the pressure diversion pipeline [19]:

$$\begin{cases} -\dfrac{\partial H}{\partial l}+\dfrac{1}{gA}\dfrac{\partial Q}{\partial t}+\dfrac{fQ^2}{2gDA^2}=0 \\ \dfrac{\partial H}{\partial t}-\dfrac{a^2}{gA}\dfrac{\partial Q}{\partial l}=0 \end{cases} \tag{2}$$

where H, Q, l, A, f, and D are the water head, the flow rate, the length, the cross-sectional area, coefficient of friction loss, and the diameter of the pipeline, respectively; g is the gravity constant. The water hammer transfer function using Eq .(2) is obtained as:

$$G_m(s)=\frac{H_m(s)}{Q_m(s)}=-2th\left(0.5T_r s\right) \tag{3}$$

where T_r is the phase length of the water hammer. In this study, the rigid water hammer model is used based on Eq. (3), which is derived as:

$$G_m(s)=-T_w s \tag{4}$$

where T_w is the flow inertia time constant.

2.1.2 Hydro-turbine and governor

The linear hydro-turbine model is generally used to describe its dynamic characteristics. The flow and torque characteristics of this model under steady conditions are [20, 21]:

$$\begin{cases} M_t=M_t(H,n,Y) \\ Q=Q(H,n,Y) \end{cases} \tag{6}$$

where M_t, Q, H, n and Y are the hydro-turbine output torque, the flow rate, the water head, the rotational speed and the guide vane opening of the hydro-turbine, respectively.
Utilizing Taylor expansion to Eq. (6), the flow and torque expression are rewritten as [20, 21]:

$$\begin{cases} m_t=e_{m\omega}x+e_{my}y+e_{mh}h \\ q_t=e_{q\omega}x+e_{qy}y+e_{qh}h \end{cases} \tag{7}$$

where m_t, q_t, h, x, and y are the relative torque, the relative flow rate, the relative water head, the relative rotational speed and the relative guide vane opening, respectively; $e_{m\omega}$, e_{my}, and e_{mh} are the transfer coefficients of the torque with respect to the rotational speed, the guide vane opening and the water head, respectively; $e_{q\omega}$, e_{qy} and e_{qh} are the transfer coefficients of the flow rate with respect to the rotational speed, the guide vane opening and the water head, respectively.

At present, most of the hydro-turbine governors adopt PID controller. The proportional, integral and differential deviation are linearly combined into a control variable. Its transfer function is [22]

$$y_{PID} = -K_p\omega - K_i\int_0^t \omega dt - K_d\dot{\omega} \tag{8}$$

where K_p, K_i, and K_d are the proportional gain, the integral gain, and the differential gain, respectively; ω is the deviation of the generator rotor speed.

The model of the mechanical hydraulic system is shown in Fig. 2. From Fig. 2, the control of the guide vane opening is described by the transfer functions of the integral link, the limitations of the acting rate and the saturation limitation.

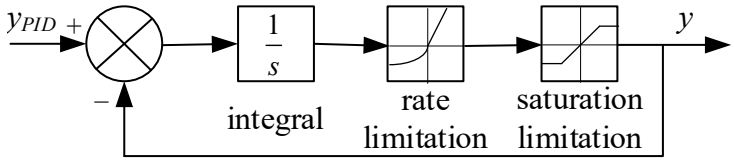

Fig. 2. The model of the mechanical hydraulic system.

2.1.3 Generator and excitation system

The third-order model of the synchronous generator is adopted in this study, which is [23]

$$\begin{cases} T'_{d0}\dfrac{dE'_q}{dt} = E_f - E'_q - I_d\left(X_d - X'_d\right) \\ T_a\dfrac{d\omega}{dt} = M_t - M_e - D_0\omega \\ \dfrac{d\delta}{dt} = \omega_0\left(\omega - 1\right) \end{cases} \tag{9}$$

where T'_{d0} is the d-axis transient open time constant of the generator; E'_q is the q-axis transient potential; E_f is the excitation voltage; I_d is the stator current; X_d is the d-axis transient reactance; X'_d is the d-axis sub-transient reactance; T_a is the inertia time constant of the generator; ω and δ are the rotor angular velocity and the rotor electrical angle, respectively; M_t and M_e are the hydro-turbine output torque and the electromagnetic torque, respectively; D_0 is the damping coefficient; ω_0 is the rotor rated angular velocity.

The excitation system regulates the terminal voltage of the synchronous generator. Its transfer function is [24]

$$\frac{V_{fd}}{E_f} = \frac{1}{K_e + sT_e} \tag{10}$$

where V_{fd}, K_e, and T_e are the voltage, the gain factor and the time constant of the exciter, respectively.

2.2 Wind power system

2.2.1 The captured power of the wind turbine

The power captured by the wind turbine is related to air density, wind passage area, and wind speed. The air density and the wind passage area are constant parameters. From Betz' Law [25], the wind speed acting on the blade of the wind turbine is the average of the wind speed at the upstream and downstream positions. The captured power and the power coefficient of the wind turbine are modelled as [26]:

$$\begin{cases} P_0 = \dfrac{1}{2}\rho A_0 C_P V^3 \\ C_P = \dfrac{\left(1+\dfrac{V_2}{V_1}\right)\left[1-\left(\dfrac{V_2}{V_1}\right)^2\right]}{2} \end{cases} \tag{11}$$

where P_0 is the wind turbine absorption power; ρ is the air density; A_0 is the wind passage area; C_P is the power coefficient; V is the wind speed acting on the wind turbine blade; V_1 and V_2 are the wind speed at the upstream and downstream positions of the blade, respectively.

2.2.2 Wind turbine maximum power tracking

The maximum power of the wind turbine needs to be tracked to make full use of wind energy. The tip speed ratio λ and the blade pitch angle θ are the two main adjustable values to realize this tracking function. The relationship among the power coefficient C_p, the pitch angle λ and the tip speed ratio θ is [26]

$$C_P(\lambda,\theta) = 0.73\left(\frac{151}{\lambda_1} - 0.58\theta - 0.002\theta^{2.14} - 13.2\right)\exp\left(\frac{-18.4}{\lambda_1}\right) \tag{12}$$

where $\lambda_1 = \dfrac{1}{\left(\dfrac{1}{\lambda\text{-}0.02}\right)+\left(\dfrac{0.003}{\theta^3+1}\right)}$.

From Eq. (12), the characteristic curves of C_P and λ with different θ are obtained in Fig. 3. From Fig. 3, power tracking is achieved by controlling the tip speed ratio λ with the pitch angle θ.

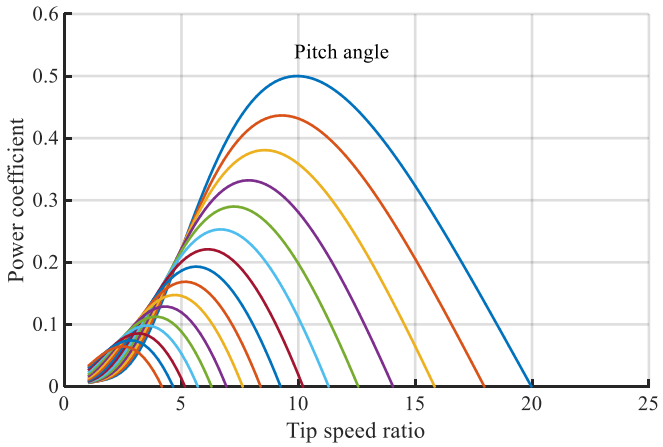

Fig. 3. The power coefficient C_P versus the tip speed ratio λ. The solid line with different colors refers to the characteristic curve of C_P with different the blade pitch angle θ.

2.2.3 Doubly-fed asynchronous generator

A doubly-fed asynchronous generator is used in this study. The current-voltage equation, the flux equation, and the electromagnetic torque equation of the rotor winding distributed in the *d-q* axis are [27]

$$\begin{cases} u_{ds} = -R_s i_{ds} + \omega_s \left[\left(L_{s\sigma} + L_m \right) i_{qs} + L_m i_{qr} \right] \\ u_{qs} = -R_s i_{qs} - \omega_s \left[\left(L_{s\sigma} + L_m \right) i_{ds} + L_m i_{dr} \right] \\ u_{dr} = -R_r i_{dr} + s\omega_s \left[\left(L_{r\sigma} + L_m \right) i_{qr} + L_m i_{qs} \right] \\ u_{qr} = -R_r i_{qr} - s\omega_s \left[\left(L_{r\sigma} + L_m \right) i_{dr} + L_m i_{ds} \right] \end{cases}, \tag{13}$$

$$\begin{cases} \psi_{ds} = -\left(L_{s\sigma} + L_m \right) i_{ds} - L_m i_{dr} \\ \psi_{qs} = -\left(L_{s\sigma} + L_m \right) i_{qs} - L_m i_{qr} \\ \psi_{dr} = -\left(L_{r\sigma} + L_m \right) i_{dr} - L_m i_{ds} \\ \psi_{qr} = -\left(L_{r\sigma} + L_m \right) i_{qr} - L_m i_{qs} \end{cases}, \tag{14}$$

and

$$T_0 = \psi_{qr} i_{dr} - \psi_{dr} i_{qr} . \tag{15}$$

u, R, i and L are the voltage, the resistance, the current and the inductance, respectively; subscripts d, q, s, r and σ represent the d-axis, the q-axis, the stator, the rotor and the magnetic leakage, respectively; ψ is the magnetic flux; T_0 is the electromagnetic torque; ω_s is the stator-to-rotor angular velocity difference; L_m is the inductance component mutual.The rotor-side and the stator-side windings of the doubly-fed asynchronous generator are both connected to the grid. Hence, different to the power model of synchronous generator, the power model of asynchronous generator equation is [27]

$$\begin{cases} P = u_{ds} i_{ds} + u_{qs} i_{qs} + u_{dr} i_{dr} + u_{qr} i_{qr} \\ Q = u_{qs} i_{ds} - u_{ds} i_{qs} + u_{qr} i_{dr} - u_{dr} i_{qr} \end{cases} \tag{16}$$

where P is the active power; Q is the reactive power.

2.3 PVPG model

2.3.1 Photovoltaic cell

The photovoltaic cell consists of a current source, an equivalent diode, an internal shunt resistor, and an internal series resistor. Its equivalent circuit is shown in Fig. 4.

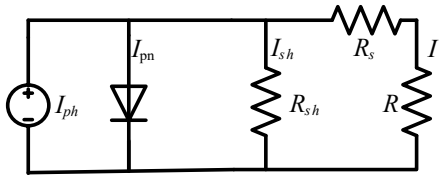

Fig. 4. The equivalent circuit of the photovoltaic cell. I_{ph} is the current of the photovoltaic cell illuminated by the solar irradiation; I_{pn} is the current flowing through the diode; I_{sh} is the current flowing through the internal shunt resistor; I is the output current of the photovoltaic cell; R_s is the internal series resistance; R_{sh} is the bypass resistance; R is the equivalent resistance of photovoltaic cells.

From Fig. 4, the output current of the photovoltaic cell I is [28]

$$I = I_{ph} - I_{pn} - I_{sh} \tag{17}$$

where I_{ph} is the current of the photovoltaic cell illuminated by the solar irradiation; I_{pn} is the current flowing through the diode, and its value indicates the ability of the P-N junction to discharge current

in the photovoltaic cell; I_{sh} is the current flowing through the internal shunt resistor. The expressions of I_{pn} and I_{sh} are

$$\begin{cases} I_{pn} = I_0 \left[\exp(\dfrac{qV_o + qIR_s}{A_c kT}) - 1) \right] \\ I_{sh} = \dfrac{V_o + IR_s}{R_{sh}} \end{cases} \tag{18}$$

where I_0 is the reverse saturation current of the diode; q is Coulomb constant; V_o is the output voltage; A_c is the P-N junction curve constant; k is Boltzmann constant; T is the absolute temperature of the photovoltaic cell. R_s is the internal series resistance; R_{sh} is the bypass capacitor.

The current I_{sh} through the parallel resistor is much smaller than the output current I of the photovoltaic cell, thus I_{sh} is negligible. The internal series resistance is much smaller than the forward conduction resistance of the diode, thus I_{sh} is approximately equal to the short-circuit current of the photovoltaic cell. Thus, based on the two approximations, Eq. (17) is rewritten as:

$$\begin{cases} I = I_{sc} \left[1 - C_1 \left(\exp\left(\dfrac{V_o}{C_2 V_{oc}} \right) - 1 \right) \right] \\ C_1 = \left(1 - \dfrac{I_m}{I_{sc}} \right) \exp\left(- \dfrac{V_m}{C_2 V_{oc}} \right) \\ C_2 = \left(\dfrac{V_m}{V_{oc}} - 1 \right) \left[\ln\left(1 - \dfrac{I_m}{I_{sc}} \right) \right]^{-1} \end{cases} \tag{19}$$

where I_{sc} and V_{oc} are the short-circuit current and the open-circuit voltage, respectively; I_m and V_m are the current and voltage at the maximum power point of the photovoltaic cell, respectively. The four parameters reflect the operating characteristics of the photovoltaic cell and determine its output characteristic curve.

2.3.2 Maximum power point tracking

The maximum power point tracking maximizes the utilization of solar energy. Traditional linear controllers cannot track the maximum output power constantly because of the complex characteristics of the internal resistance in the photovoltaic cells. Hence, the conductance increment method [29] is used in this study to achieve maximum power point tracking, and the power calculation formula $P=UI$ is derived from both sides as [30]:

$$\frac{dP}{dU} = I + U\frac{dI}{dU} \tag{20}$$

As shown in Fig. 5, when dP/dU is equal to 0, the PVPG is working on the maximum power point. When dP/dU is less than 0, the voltage is lowered to reach the maximum power point. When dP/dU is greater than 0, the maximum power point is reached by increasing the voltage. The flow chart of conduction increment method is shown in Fig. 6 where n represents the discretization point in the time.

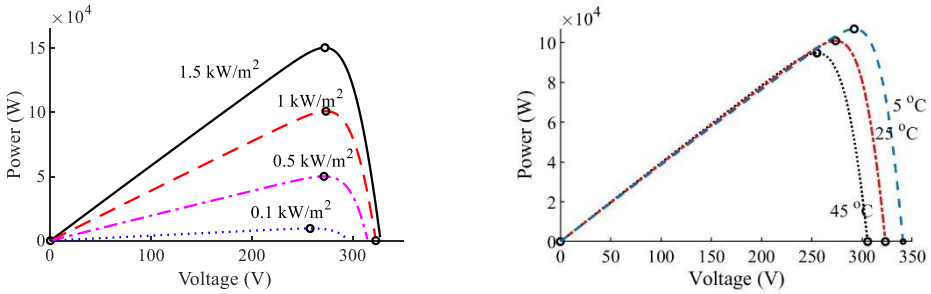

(a) Solar radiation irradiation characteristic (b) Temperature characteristic

Fig. 5. The output power versus voltage with different solar radiation irradiation and temperature.

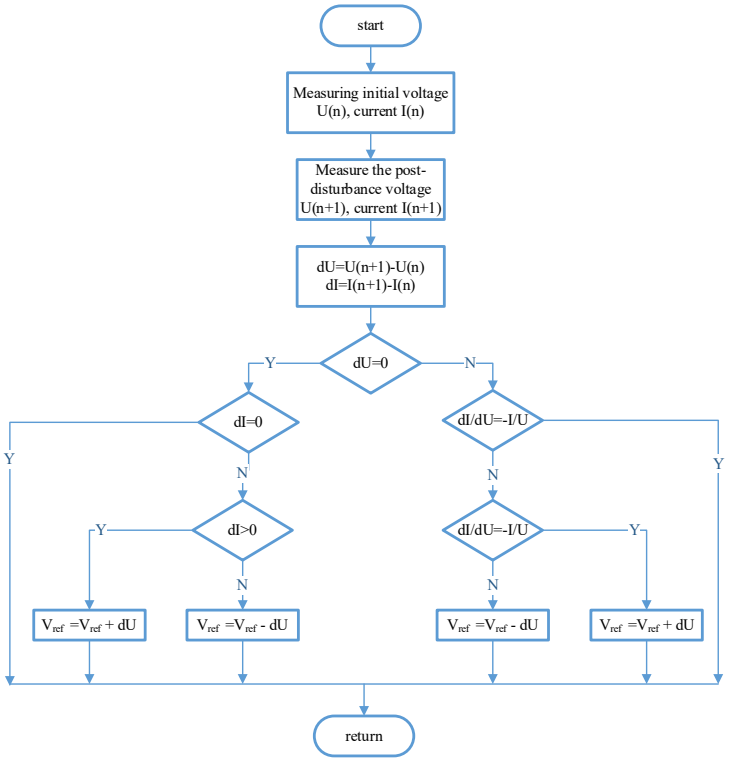

Fig. 6. The flow chart of conduction increment method.

3. Simulation results

3.1 Meteorological data input

In this study, the output of wind power and photovoltaic power are affected by climate factors like wind speed, solar irradiation and temperature. Hence, six typical scenarios are used to verify the applicability and universality of the proposed model. The scenarios have been selected to represent some extreme cases in a typical climate year of northern China [31] such as maximum daily average wind speed occurring on January 3, the minimum of daily average solar irradiation occurring on April 1 and so on as shown in Table 1.

irradiationThe daily variations of wind speed, solar irradiation and temperature under six different scenarios are shown in Fig. 7.

Table 1 Meteorological data of selected 6 days in a typical climate year for Beijing [30]

Significance	Scenario	Average wind speed (m/s)	Average solar irradiation (W/m^2)	Average temperature (℃)
Daily average wind speed	Jan. 3	6.18	97.92	-3.85

maximum				
Daily average temperature minimum	Jan. 18	4.82	128.70	-9.73
Daily average solar irradiation minimum	Apr. 1	4.02	0.00	7.73
Daily average solar irradiation maximum	May. 19	3.74	334.72	22.26
Daily average temperature maximum	Jun. 22	4.01	238.31	35.01
Daily average wind speed minimum	Nov. 21	0.41	100.81	5.42

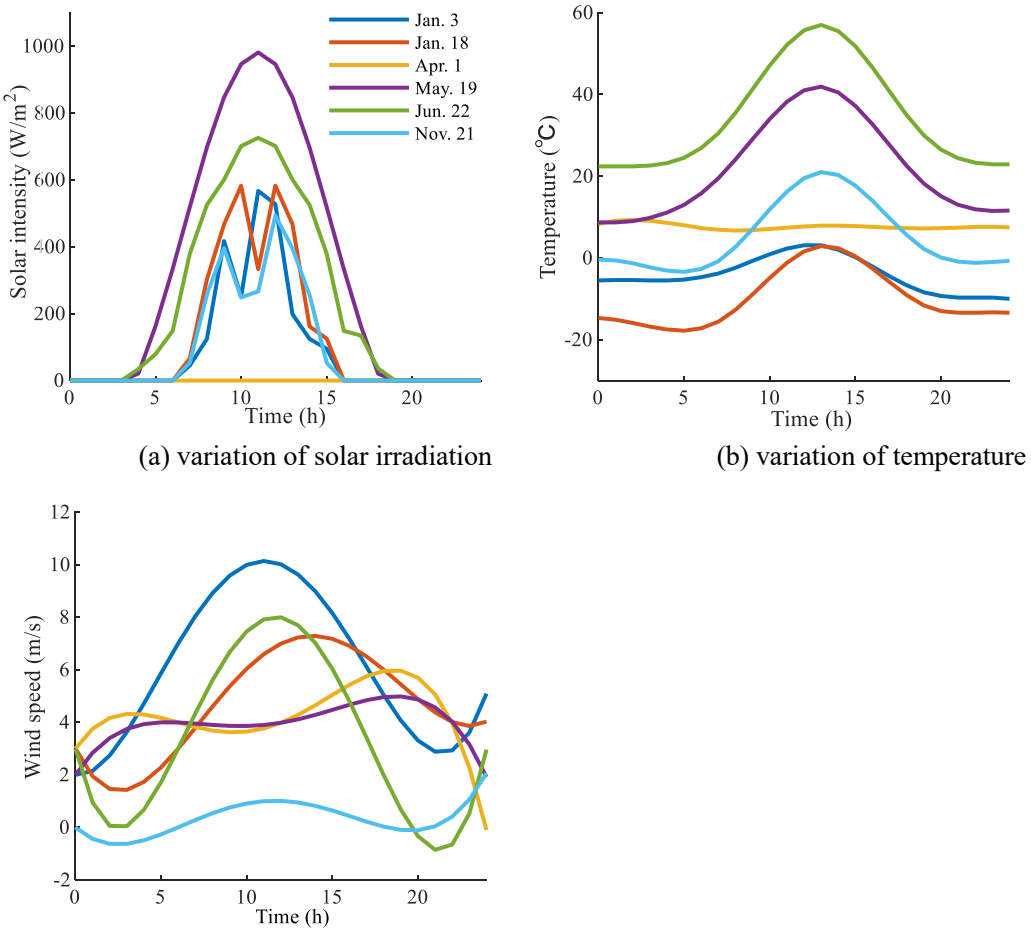

(a) variation of solar irradiation

(b) variation of temperature

(c) variation of wind speed

Fig. 7. The daily variation curve of selected 6 days in a typical climate year for Beijing.

The hourly climate data of six scenes in Fig. 7 is imported into the established model of HWPS. The parameter values of the model are shown in Table 2. The 4th Runge-Kutta method is used to solve numerical the proposed model. The simulation step length used is 2.0×10^{-4}s, and the simulation duration is 24 hours. The output power variations of WPG and PVPG with or without HPG compensation are shown in Fig. 8.

Table 2 The parameter values of HWPS

Symbol	Parameter	Unit	Numerical

K_p	The proportional gain		1.6
K_i	The integral gain		0.25
K_d	The differential gain		1
b_p	Constant state slip coefficient		0.01
A_t	Turbine gain coefficient		1.15
D_t	Damping coefficient of angular velocity deviation		5
f_p	Head loss coefficient		0.0028
q_{nl}	Relative value of no-load flow	p.u.	0.15
T_f	Start time of servo relay	s	10
T_g	Relay shutdown time of follow-up system	s	20
Tr	Low pass filter time constant	s	0.02
E_{fmax}	Maximum output value of regulator	p.u.	11.5
E_{fmin}	Minimum output value of regulator	p.u.	-11.5
V_{t0}	Initial value of terminal voltage	p.u.	1
V_{f0}	Initial value of excitation voltage	p.u.	10.28
X_d	*d*-axis transient reactance	p.u.	1.132
$X_{d'}$	*d*-axis sub-transient reactance	p.u.	0.291
X_q	*q*-axis transient reactance	p.u.	0.731
$X_{q''}$	*q*-axis sub-transient reactance	p.u.	0.218
L_{ls}	The stator inductance	p.u.	0.18
$R_{r'}$	Rotor resistance	p.u.	0.02
$L_{lr'}$	Rotor inductance	p.u.	0.16
L_m	Stator - rotor mutual inductance	p.u.	2.90
H	Inertia constant of doubly-fed induction motor	s	0.69
F	Friction coefficient of doubly-fed induction motor	p.u.	0.01
p	Pole logarithm of doubly-fed induction machine		3.00
P_{Vmax}	Maximum power output of photovoltaic cells	W	315.00
V_{oc}	Photovoltaic cell open circuit voltage	V	64.60
I_{sc}	Photovoltaic cell short circuit current	A	6.14
I_m	Current of photovoltaic cell at the maximum power point	A	5.76
V_m	Voltage of photovoltaic cell at the maximum power point	V	54.70
I_L	Diode saturation current of photovoltaic cell	A	6.15
R_{sh}	Bypass resistance	ohms	430.00
R_s	Internal series resistance	ohms	0.43
$D_{in}\backslash D_{max}\backslash D_{min}$	The initial, maximum and minimum value of duty cycle	p.u.	0.485\0,6\0.4
D_{eltaD}	MPPT disturbance quantity		*2.00E-05*
L_1	Boost circuit inductance	mH	*5*
C	Boost circuit capacitance	μF	*100.00*

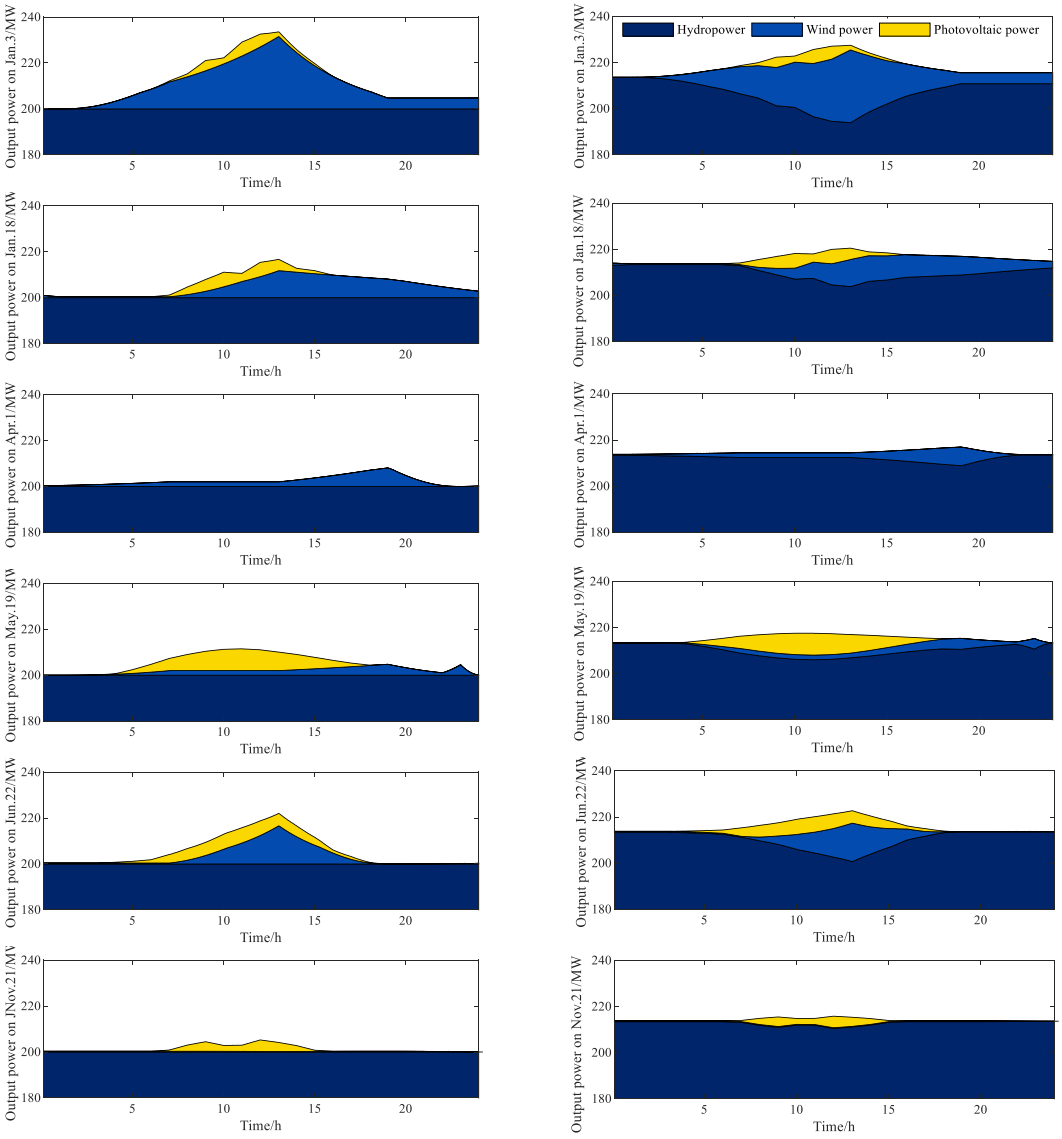

(a) HWPS output power without HPG compensation (b) HWPS output power with HPG compensation

Fig. 8. The output power variations of WPG and PVPG with or without HPG compensation.

The output power of hydropower, as shown in Fig. 8(a), is basically unchanged before the compensation, while the output power of wind power and photoelectric power changes due to the variations of meteorological conditions. The output power of hydropower, as shown in Fig. 8(b), decreases with the increase of the output power generated from wind and photoelectric systems. The compensation allows to reduce the power fluctuation from the wind and photoelectric system. So HWPS output power with HPG compensation is more stable than HWPS output power without HPG compensation.

3.2 Power spectral density

Traditional methods use a random variable from a statistical point of view or adopts autoregressive moving average time series model (ARMA). Both methods are described from a single time scale and the obtained results are not representative in special or extreme climate conditions. Power spectral density (PSD) is an alternative approach the allows to overcome the limitation of traditional methods to describe power fluctuation. The PSD is expressed in the frequency domain, which is used to describe the output fluctuation components in different

frequency scales. According to Rayleigh energy theorem, the sum of squares (or integrals) of functions is equal to the sum of squares of Fourier transform [32], which is

$$\int_{-\infty}^{+\infty} |x(t)|^2 dt = \int_{-\infty}^{+\infty} |X(f)|^2 df \tag{21}$$

where $X(f)$ is the continuous Fourier transform of $x(t)$; f is the frequency component of x.

According to the simulation power results in Section 3.1, the power spectrums of WPG, PVPG and HWPS with HPG compensation are obtained by Welch power spectrum estimation method [33], which are shown in Fig 8.

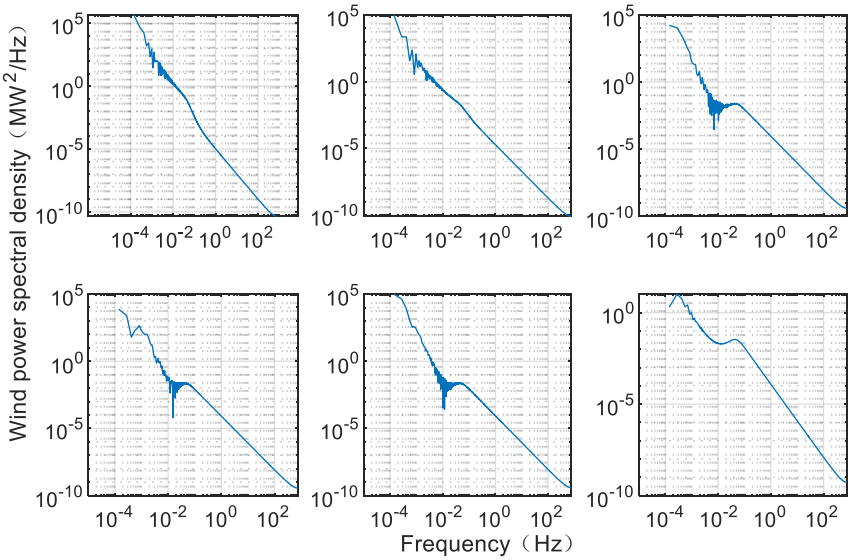

(a) Wind power spectrum density

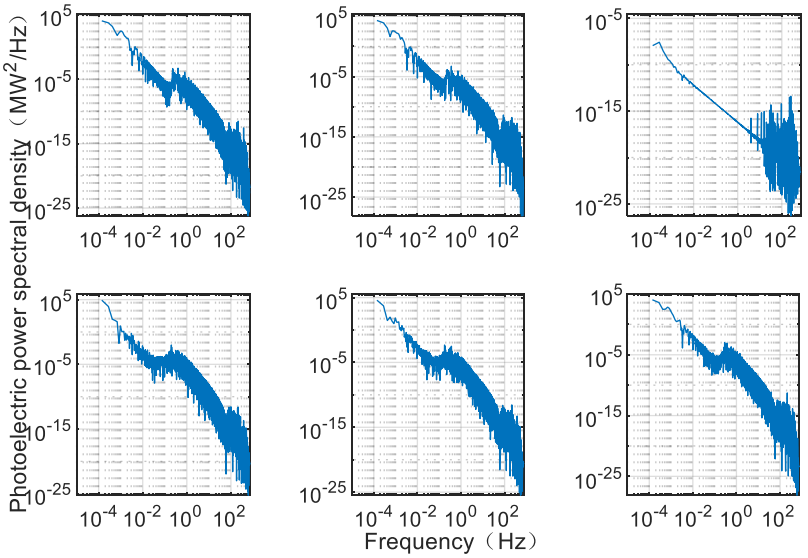

(b) Photoelectric power spectrum density

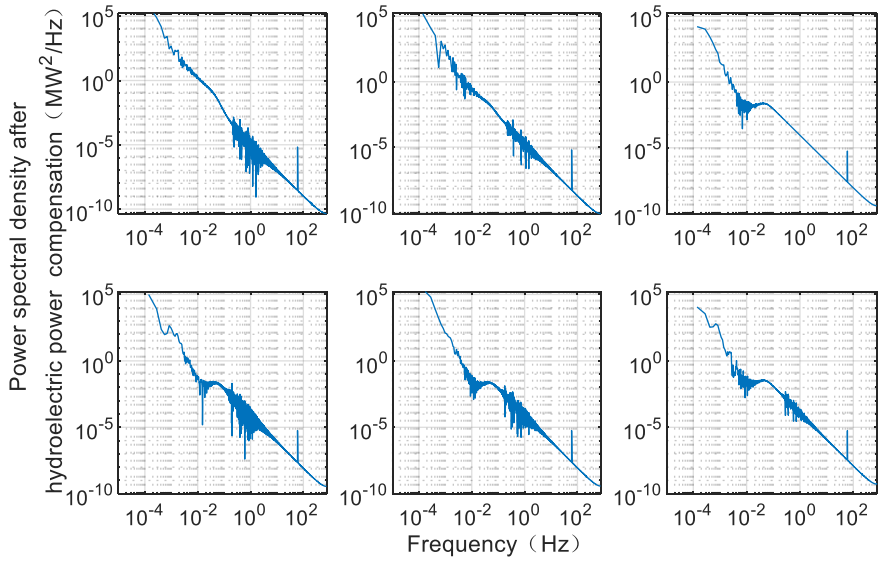

(c) HWPS with HPG compensation power spectrum density

Fig. 9. The power spectrum density of WPG, PVPG and HWPS with HPG compensation.

Fig. 9 shows the PSD for wind power, photovoltaic power and HWPS with HPG compensation. From Fig. 9(a), the PSD of wind power oscillates to different degrees at 10^{-3}Hz to 10^{-1}Hz. From Fig. 9(b), the PSD range to PVPG's vibration zone is wider than that of the wind power, with varying degrees of oscillation from 10^{-3}Hz to 10^{3}Hz. From Fig. 9(c), the range of the vibration zone decreases, mainly focusing on 10^{-2}Hz to 10^{0}Hz. Compared the three figures, the PSD of six days all decreases with the increasing frequency. Differently, the PSD of PVPG oscillates more severely with the increase of frequency, and the amplitude of PSD after HPG compensation is lower than that of PVPG. Because the photoelectric excludes the moment of inertia in power generation conditions, which is vulnerable to the interference of electronic components. While this interference is reduced by the compensation of HPG, as demonstrated in Fig. 9(c).

3.3 Analysis of complementary characteristics

The commonly used evaluation indexes of electric power system include the load loss probability, the expectation of load loss probability, the maximum output power ratio and the peak capacity ratio. However, due to the characteristics of the multi-time scales, non-stationary and nonlinear for WPG and PVPG, the above indexes are insufficient to indicate the output characteristics of HWPG. Therefore, this study proposes the power stability index and complementary index which are more suitable for HWPG.

3.3.1 Stability analysis

The stability of WPG and PVPG output power influences the security and stability of power grid operation. The power stability index, I_s, is used to quantify the degree of power fluctuation, which is

$$I_S = \frac{1}{n-1}\sum_{i=1}^{n-1}\left|\frac{P_{i+1}-P_i}{P_c}\right|. \tag{22}$$

where n is the total number of samples; P_i is the output power at the i^{th} sampling point; P_c is the installed capacity. A larger value of I_s indicates a better stability performance of the system.

According to the simulation power results in Section 3.1 and Eq. (22), the power stability index of wind power, photoelectric power, with or without hydropower compensation for different scenarios are shown in Figure 10.

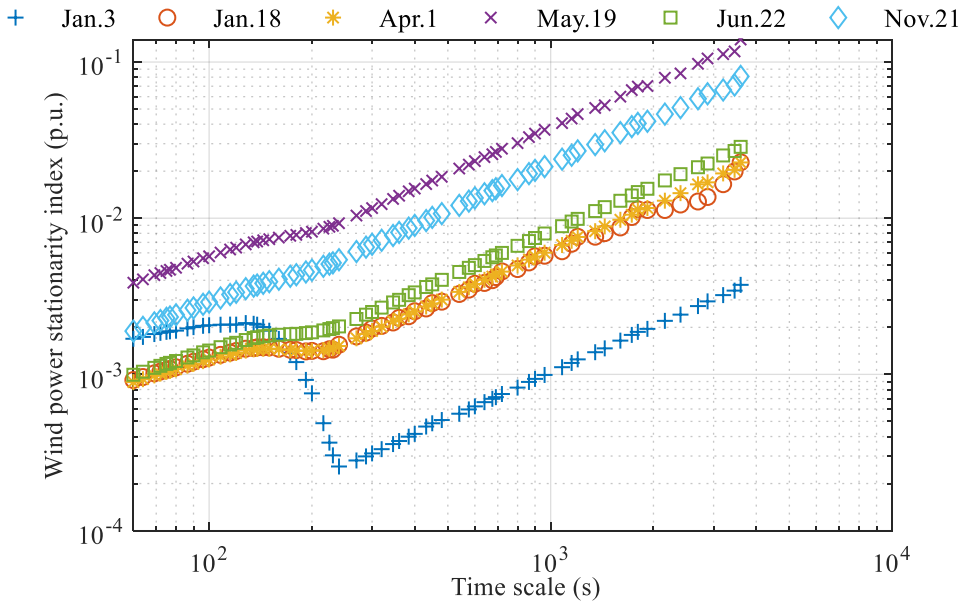

(a) The power stability index of wind power

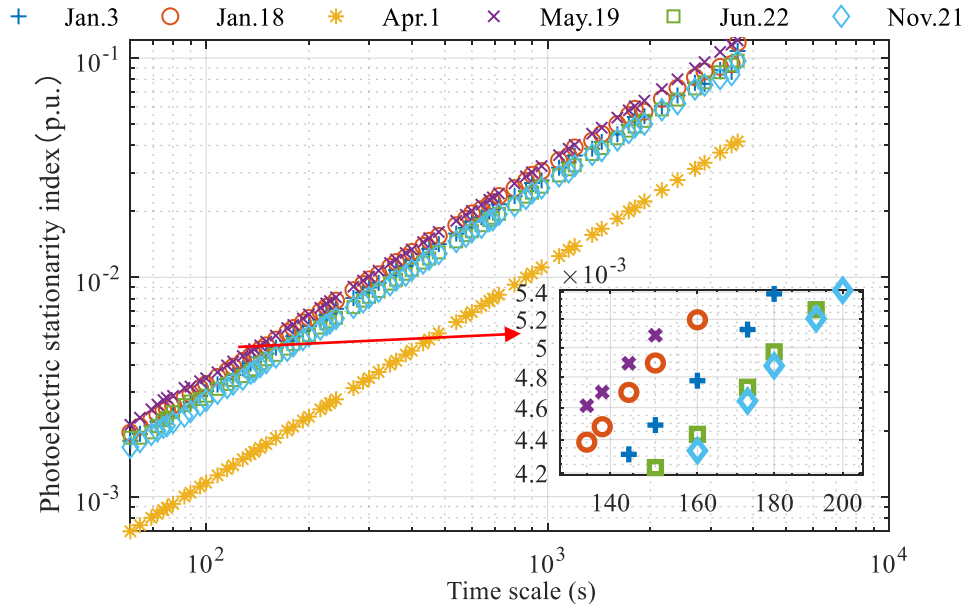

(b) The power stability index of photoelectric power

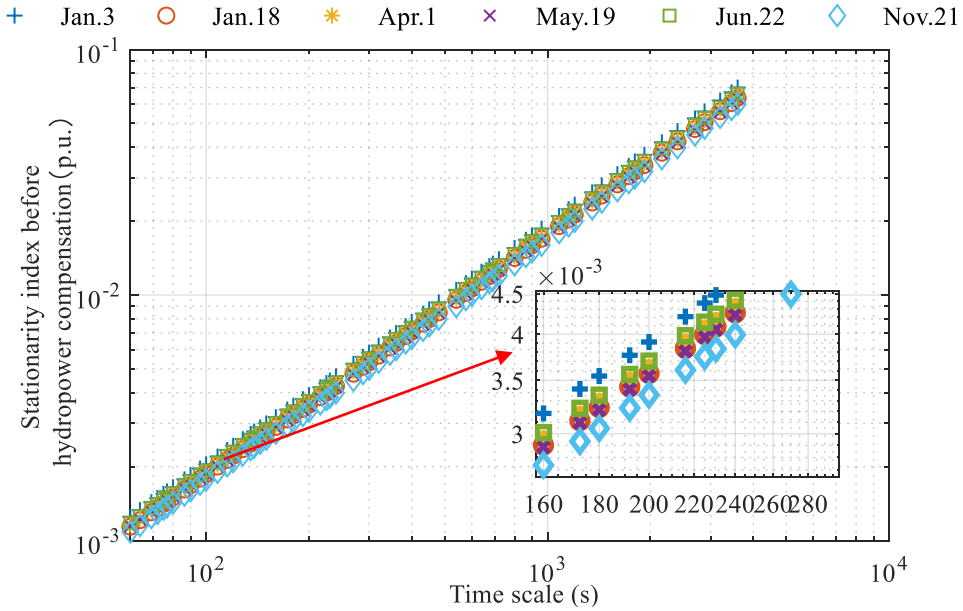

(c) The power stability index without hydropower compensation

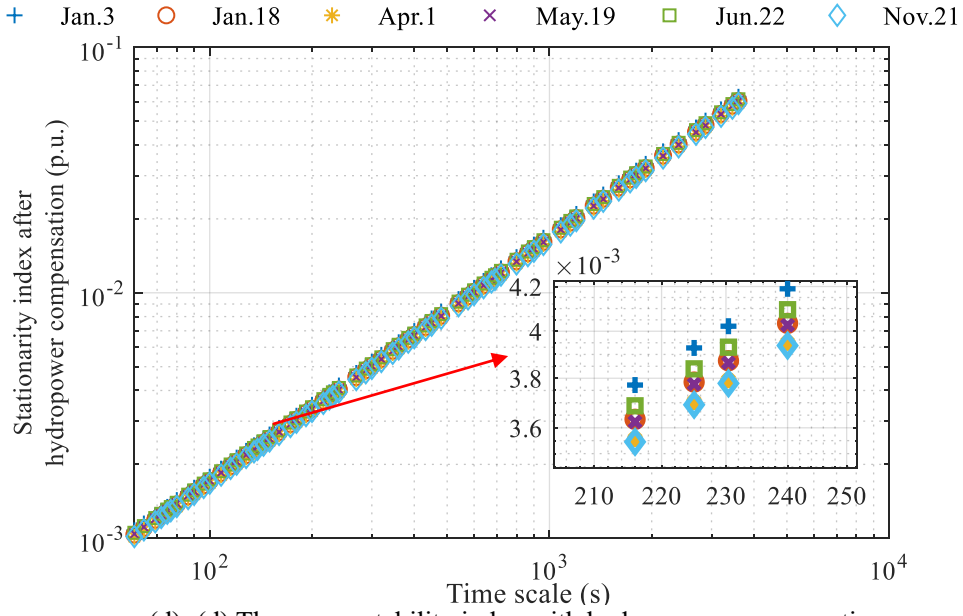

(d) (d) The power stability index with hydropower compensation

Fig. 10. The power stability index in different scenes.

As shown in Fig. 10(a), to the scenario of Jan. 3, the stability index increases slowly from $10^{1.6}$s to $10^{2.1}$s, and then decreases rapidly from $10^{2.1}$s to $10^{2.2}$s. The inflection point appears around $10^{2.2}$s and then starts to increase again. To the other five scenarios, the stability index of WPG continuously increases with the increase of time scale. The stability index of PVPG increases with the increase of time scale on different scenarios (Fig. 10(b)), and the stability index on Apr. 1 is lower than that of other analyzed scenarios. From Figs. 10(c, d), the change trend of the stability index which is proportional to the time scale, is consistent with or without the hydropower compensation, and the stability index with the hydropower compensation is smaller than that without the hydropower compensation. In addition, the stability index is small on the days with low wind speed and solar irradiation, such as Jan. 3 and Apr. 1. This is because the output power of PVPG and WPG are small in those two days, leading to relatively small power fluctuations.

3.3.2 Complementarity analysis

Complementary index I_C is adopted to quantify the degree of power complementation between

different generation systems. The larger value of I_C indicates a better complementary performance of the system. The complementary index is defined as:

$$I_C = \frac{1}{n-1}\sum_{i=1}^{n-1}\left|\frac{P_{h,i+1}-P_{h,i}}{T}+\frac{P_{w,i+1}-P_{w,i}}{T}+\frac{P_{s,i+1}-P_{s,i}}{T}\right| \tag{23}$$

where $P_{h,i}$, $P_{w,i}$ and $P_{s,i}$ are the output power of HPG, WPG and PVPG at the i^{th} sampling point, respectively; T is the sampling data period.

According to the simulation power results in Section 3.1 and Eq. (23), the power complementarity index between and among hydropower, wind power and photoelectric power in different time scales are shown in Fig. 11.

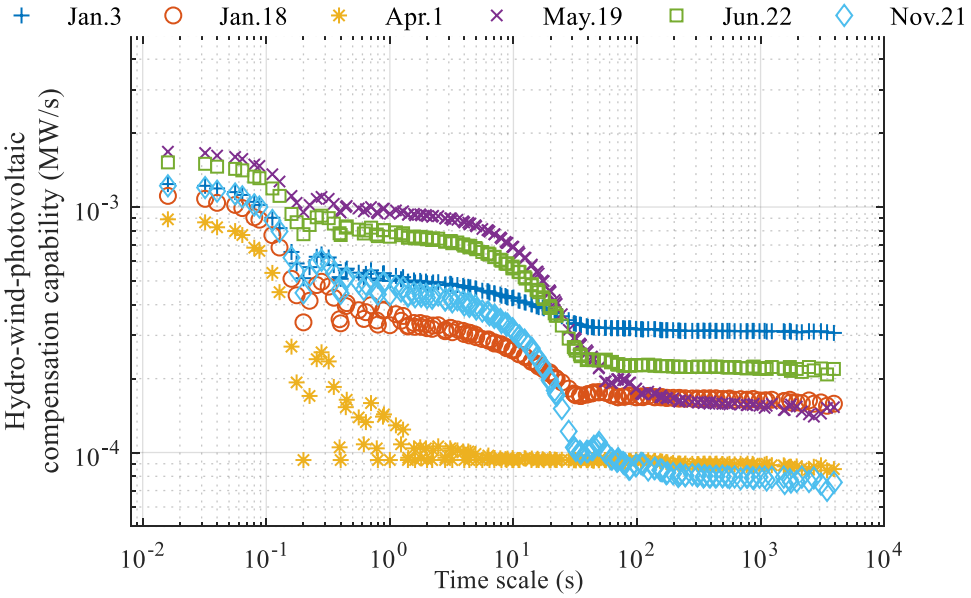

(a) The power complementary index I_c of hydro-wind-photovoltaic

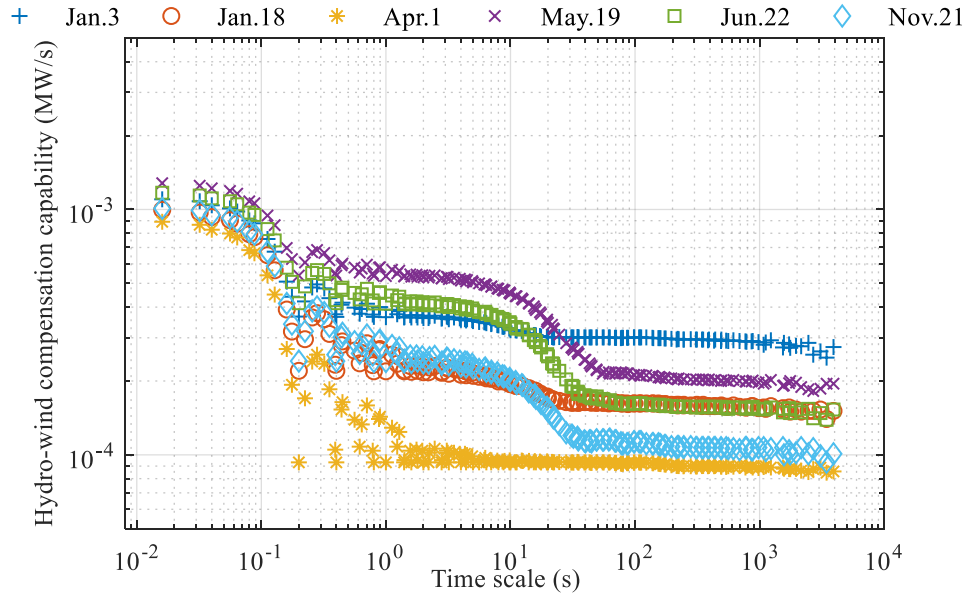

(b) The power complementary index I_c of hydro-wind

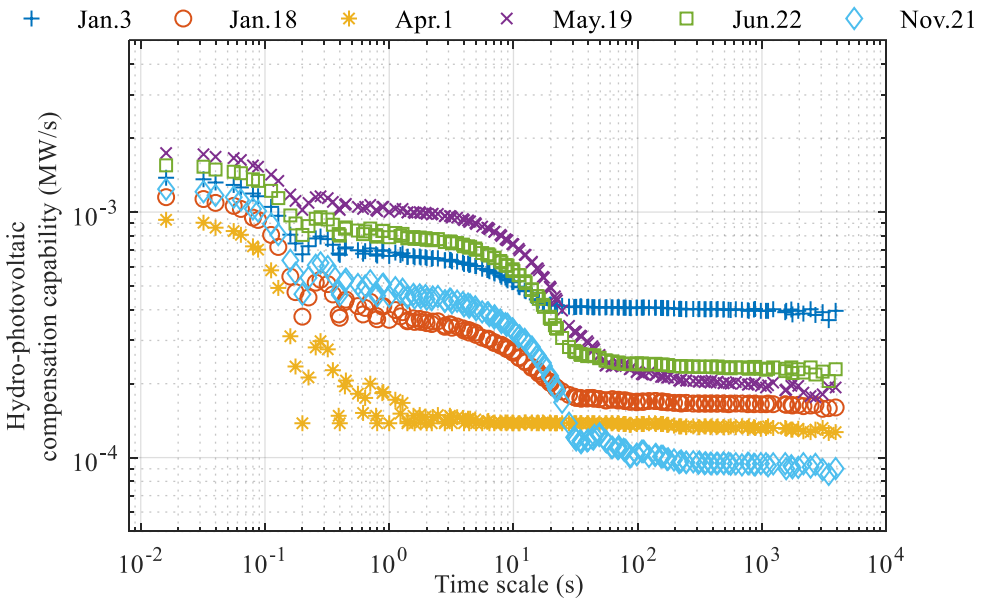

(c) The power complementary index I_c of hydro-photovoltaic

Fig. 11. The power complementary index I_c characteristics in different date scenes.

By comparing Figs. 11(a, b, c), the complementary index with the hydropower compensation is mainly divided into five parts, among which, (10^{-2}, 10^{-1}) seconds, ($10^{0.5}$, 10^{1}) seconds and ($10^{1.5}$, $10^{3.3}$) seconds remain unchanged with the increase of time scale. Interestingly, (10^{-1}, $10^{0.5}$) seconds and (10^{1}, $10^{1.5}$) decrease with the increase of time scale. The hydropower unit controls the increase and decrease of active power by primary and secondary frequency modulation to keep the system frequency stable. Adjusting the power fluctuation within 3s and fast response are the characteristic of primary frequency modulation. From Fig. 11, the complementary index I_C decrease on the time scale of (10^{-1}, 10^{1}) seconds, i.e. the hydropower units operating in the primary frequency modulation. With the increase of time scale, the fluctuations with long cycle (generally 10s to 1min) are regulated by secondary frequency modulation. From Fig. 11 the complementary index I_C decrease on the time scale of (10^{1}, $10^{1.5}$) seconds when the hydropower units operates in the secondary frequency modulation.

4. Conclusions

The problem of the output fluctuation of wind and photovoltaic power generation system can be effectively solved by the power compensation through hydroelectric power generation system.

The stability of integrated hybrid generation systems has been analysis in this paper. This has been obtained using power spectral density, stationarity index and complementary index and comparing different climate conditions (scenarios). The stability and complementarity of output power of hydro-wind-photovoltaic system has been analyzed under different time scales using the proposed evaluation indexes. The results obtained show that the power spectral density of the hydro-wind-photovoltaic system is a combination of general linear attenuation characteristics of the wind power system and the oscillation characteristics in middle frequency of the photovoltaic power generation system. It has been observed that the high-frequency power spectrum density of hydro-wind-photovoltaic system has no oscillation, which indicates that it plays a good role in power compensation on the daily time scale.

Frequent changes of the wind speed or solar irradiation affect the stationarity of the power production systems and in particular for larger the time scale. Including hydropower system, the stability of the overall system can be effectively improved and tends to be consistent under different scenarios, which reflects the advantages of the hydro-wind-photovoltaic system and contribute to the utilization of renewable energy.

Acknowledgements

This research is supported by the scientific research foundation of the Natural Science Foundation of Shaanxi Province of China (2019JLP-24), Shaanxi Science and Technology Innovation Team, and Water Conservancy Science and Technology Program of Shaanxi Province (2018slkj-9).

References:

1. Sterl S, Vanderkelen I, Chawanda CJ, Russo D, Brecha RJ, van Griensven A, et al. Smart renewable electricity portfolios in West Africa. Nature sustainability. 2020;3:710-719.
2. Kheshti M, Ding L, Nayeripour M, Wang X, Terzija V. Active power support of wind turbines for grid frequency events using a reliable power reference scheme. RENEW ENERG. 2019;139:1241-1254.
3. Mak D, Choeum D, Choi DH. Sensitivity analysis of volt-VAR optimization to data changes in distribution networks with distributed energy resources. APPL ENERG. 2020;261.
4. Neto PJDS, Barros TAS, Silveira JPC, Filho ER, Guerrero JM. Power management techniques for grid-connected DC microgrids: A comparative evaluation. APPL ENERG. 2020;269:115057.
5. Guo B, Su M, Sun Y, Wang H, Liu B, Zhang X, et al. Optimization Design and Control of Single-Stage Single-Phase PV Inverters for MPPT Improvement. IEEE T POWER ELECTR. 2020;35:13000-13016.
6. Sun L, Guo P, Luo X. Numerical investigation on inter-blade cavitation vortex in a Franics turbine. RENEW ENERG. 2020;158.
7. Beres RN, Wang X, Liserre M, Blaabjerg F, Bak CL. A Review of Passive Power Filters for Three-Phase Grid-Connected Voltage-Source Converters. IEEE J EM SEL TOP P. 2016;4:54-69.
8. Kumar A, Gupta V, Patel N, Gupta N, Babu BC. Improved robust-mixed-norm-based controller for grid-tied PV systems under voltage disturbances. IET Generation, Transmission & Distribution. 2020;14:2610-2619.
9. Song Z, Park H, Delgado FP, Wang H, Li Z, Hofmann HF, et al. Simultaneous Identification and Control for Hybrid Energy Storage System Using Model Predictive Control and Active Signal Injection. IEEE T IND ELECTRON. 2020;67:9768-9778.
10. Ariyaratna P, Muttaqi KM, Sutanto D. A novel control strategy to mitigate slow and fast fluctuations of the voltage profile at common coupling Point of rooftop solar PV unit with an integrated hybrid energy storage system. Journal of Energy Storage. 2018;20:409-417.
11. Ciupageanu D, Barelli L, Lazaroiu G. Real-time stochastic power management strategies in hybrid renewable energy systems: A review of key applications and perspectives. ELECTR POW SYST RES. 2020;187:106497.
12. Zhao X, He J, Fu B, He L, Xu G. A System Compensation Based Model Predictive AGC Method for Multiarea Interconnected Power Systems with High Penetration of PV System and Random Time Delay between Different Areas. MATH PROBL ENG. 2018;2018:1-10.
13. Short-Term Optimal Operation of a Wind-PV-Hydro Complementary Installation: Yalong River, Sichuan Province, China. ENERGIES. 2018;11:868.
14. Lamedica R, Santini E, Ruvio A, Palagi L, Rossetta I. A MILP methodology to optimize sizing of PV - Wind renewable energy systems. ENERGY. 2018;165:385-398.
15. Niu D, Zhen H, Yu M, Wang K, Sun L, Xu X. Prioritization of Renewable Energy Alternatives for China by Using a Hybrid FMCDM Methodology with Uncertain Information. SUSTAINABILITY-BASEL. 2020;12:4649.
16. Banerjee S, Dasgupta K, Chanda CK. Short term hydro – wind – thermal scheduling based on particle swarm optimization technique. INT J ELEC POWER. 2016;81:275-288.
17. Levieux LI, Inthamoussou FA, De Battista H. Power dispatch assessment of a wind farm and a hydropower plant: A case study in Argentina. ENERG CONVERS MANAGE. 2019;180:391-400.
18. Wang X, Chang J, Meng X, Wang Y. Hydro-thermal-wind-photovoltaic coordinated operation considering the comprehensive utilization of reservoirs. ENERG CONVERS MANAGE. 2019;198:111824.

19. Wang X, Chang J, Meng X, Wang Y. Hydro-thermal-wind-photovoltaic coordinated operation considering the comprehensive utilization of reservoirs. ENERG CONVERS MANAGE. 2019;198:111824.
20. Li H, Chen D, Zhang X, Wu Y. Dynamic analysis and modelling of a Francis hydro-energy generation system in the load rejection transient. IET RENEW POWER GEN. 2016;10:1140-1148.
21. Li H, Chen D, Zhang H, Wang F, Ba D. Nonlinear modeling and dynamic analysis of a hydro-turbine governing system in the process of sudden load increase transient. MECH SYST SIGNAL PR. 2016;80:414-428.
22. Xu B, Wang F, Chen D, Zhang H. Hamiltonian modeling of multi-hydro-turbine governing systems with sharing common penstock and dynamic analyses under shock load. ENERG CONVERS MANAGE. 2016;108:478-487.
23. Zhang H, Chen D, Xu B, Wang F. Nonlinear modeling and dynamic analysis of hydro-turbine governing system in the process of load rejection transient. ENERG CONVERS MANAGE. 2015;90:128-137.
24. "IEEE Draft Recommended Practice for Excitation System Models for Power System Stability Studies," in IEEE P4215/d38, October, (2015).
25. Tavares JM, Patrício P. Maximum thermodynamic power coefficient of a wind turbine. WIND ENERGY. 2020;23:1077-1084.
26. Murdoch A, Winkelman JR, Javid SH, Barton RS. Control Design and Performance Analysis of a 6 MW Wind Turbine-Generator. IEEE Transactions on Power Apparatus & Systems. 2007;PER-3:49.
27. Poitiers F, Bouaouiche T, Machmoum M. Advanced control of a doubly-fed induction generator for wind energy conversion. ELECTR POW SYST RES. 2009;79:1085-1096.
28. Multi-Time-Scale Coordinated Operation of a Combined System with Wind-Solar-Thermal-Hydro Power and Battery Units.
29. Zhang Y, Sun H, Guo Y. Research on maximum power point tracking method of photovoltaic power generation. J INTELL FUZZY SYST. 2019;37:3149-3162.
30. Tey KS, Mekhilef S. Modified incremental conductance MPPT algorithm to mitigate inaccurate responses under fast-changing solar irradiation level. SOL ENERGY. 2014;101:333-342.
31. China Meteorological Data Network, http://data.cma.cn/.
32. Roncallo L, Solari G. An evolutionary power spectral density model of thunderstorm outflows consistent with real-scale time-history records. J WIND ENG IND AEROD. 2020;203:104204.
33. Barbe K, Pintelon R, Schoukens J. Welch Method Revisited: Nonparametric Power Spectrum Estimation Via Circular Overlap. IEEE T SIGNAL PROCES. 2010;58:553-565.

Declaration of interests

√ The authors declare that they have no known competing financial interests or personal relationships that could have appeared to influence the work reported in this paper.